Recursive Domain Decomposition Approach in 2-D Time-Harmonic Wireless Power Transfer Simulations Considering Litz Wires

Antero Marjamäki and Paavo Rasilo

Unit of Electrical Engineering, Tampere University, FI-33100 Tampere, Finland

A recursive domain decomposition approach based on a 2-D time-harmonic finite element (FE) model with AVI formulation is used to model a wireless power transfer (WPT) unit with litz wires. Similar techniques exist in the literature, but they have not yet been applied to WPT units. The approach produces a model that is significantly faster to update and resolve than a traditional FE model, and hence, it is suitable for performing parametric sweeps where the positioning of the coils is varied. Using the technique, it is possible to study losses emerging in individual strands even with an extremely high number of strands. The loss distribution between the litz wire strands is studied, varying the number of strands from 7 to 925. The results and speed are compared with a traditional FE AVI model. The method yields the results up to a 1% relative error compared with the traditional model with significantly faster simulation time.

***Index Terms*— Domain decomposition, iterative substructuring, macroelement method, multiscale model, reduction to the interface, static condensation, wireless power transfer (WPT).**

I. Introduction

WIRELESS power transfer (WPT) systems can be used to transfer power without the need for physical contacts [1]. Wireless charging is expected to drastically improve the potential of electric vehicles. For example, parking squares and sections near traffic lights could be equipped with dynamic wireless charging coils that would boost the ranges of electric vehicles without the need for larger batteries [2]. In these kinds of applications, the WPT coils are perfectly aligned only for a short period of time, so it is crucial to analyze and optimize the operation of the windings also when the coils are badly aligned.

The WPT systems contain windings that, due to the high operation frequencies, are made of litz wires to reduce eddy-current losses. The designing of a WPT unit is a complex process. The units usually contain power electronic converters in both sending and receiving sides of the unit that needs to be dimensioned correctly. A compensation topology has to be selected, and in order to select the values for the compensation components, it is necessary to obtain certain lumped parameters, e.g., self-inductance and mutual inductance of the windings [3]. The load also affects the operation of the WPT device. On top of these considerations, there are several parameters that have a negative impact on the performance of the WPT unit. These parameters include offsets from the optimal position, variance in the distance between the windings, and misalignment of the magnetic axes of the windings.

The inductances and coupling factors, which are needed in the design process, are typically estimated using simplified formulas [4], [5], computed using a simplified 3-D or 2-D magnetic field simulations [6], [7], or just measured from a prototype system [8], [9]. After the identification, the analysis is usually carried out using equivalent circuits. This approach is suitable for system-level optimization but not enough for optimizing the actual winding geometries.

The models used in the field simulations must be simplified in such a way that individual conductors are not modeled, but the wire is considered as a homogenous block of conducting material. This simplification is necessary already in 2-D models especially if the litz wire contains a large number of strands. This simplification, however, loses a lot of the information about how eddy currents and proximity effect affect the current distribution in and between the wires. It would require the use of special techniques, such as homogenization [10]–[13], to incorporate the proximity information in the models. This information is crucial in order to optimize coil designs, improve efficiency, and avoid local overheating of the winding.

In [14], harmonic decomposition is used to simulate losses with respect to frequency since direct field simulation is found to be too heavy for daily engineering work. The heaviness of computing results through simulations prohibits the use of many optimization techniques where losses have to be simulated repeatedly with many different offsets, distances, and angles.

In this study, a WPT unit that contains two rectangular spiral windings that are made of litz wire is analyzed using a time-harmonic 2-D cross-sectional model. A recursive domain decomposition approach, where repeated domains (e.g., the winding and litz wire) are isolated, pre-processed, and reused in a recursive manner during the simulation, is proposed.

The proposed decomposition technique is presented and applied to a finite element (FE) model used to compute winding losses of a WPT system. The accuracy is verified, and the speed is compared against a traditional FE model.

Manuscript received June 18, 2020; revised September 8, 2020; accepted September 8, 2020. Date of publication September 15, 2020; date of current version October 19, 2020. Corresponding author: A. Marjamäki (e-mail: antero.marjamaki@tuni.fi).

Color versions of one or more of the figures in this article are available online at http://ieeexplore.ieee.org.

Digital Object Identifier 10.1109/TMAG.2020.3024158

The approach is based on a non-overlapping domain decomposition technique called Schur complement method [15], [16] which is sometimes called reduction to the interface, or, especially in mechanics, iterative substructuring [17], [18]. It also shares similarities with static condensation [19], and macroelement methods [20]–[22]. The relationships of the methods are discussed in [23]. The proposed technique can also be understood as a macroelement method coupled with the standard magnetic vector potential–voltage–current (AVI) formulation [24] that is used to model the current in the strands of the litz wires.

The ultimate goal is to divide the problem domain into smaller subdomains and eliminate interior regions of subdomains that, e.g., contain highly complex structures, such as windings made of litz wire. This results in a problem whose solving is faster and less resource-intensive and, thus, offers time savings when it has to be done repeatedly. To achieve this goal, domain decomposition techniques have been used in electrical machine simulations [20], [25], [26]. Model reduction methods have been studied to achieve a similar goal [27] for WPT units. However, the domain decomposition approach has not been used before to model WPT systems containing litz wires.

The subproblems are, to some extent, made independent of each other and composable in a flexible way by utilizing the mortar method with the Lagrange multipliers [28], [29]. The mortar method is slightly customized to benefit from the fact that the subdomains are closed regions with a periodic boundary. An auxiliary function space [30] that is spanned by the Fourier basis functions is used as the space for the Lagrange multipliers. For further details of the spatial decomposition technique, we refer to our earlier work [31] where we demonstrate the use of the Fourier basis for the Lagrange multiplier space in static magnetic field computations. This work extends the previous work by incorporating the time-harmonic AVI formulation and enabling the use of the method in a recursive manner to model more complex hierarchical winding structures made from stranded conductors. This is done in order to be able to compute global and local eddy-current and proximity losses in the litz wire windings of WPT systems.

The decomposition is done at the earliest step by identifying the repeated geometrical entities and utilizing the problem geometry. All domains are meshed independently of each other instead of meshing the total problem first and dividing the elements and degrees of freedom (DOF) after discretization. This enables aggressive reusing and caching of all precomputed data. Using the mortar method, this precomputed data can be used in several places and embedded in multiple ways when the total problem is assembled. The circuit equations modeling the strand currents are coupled into the reduced Schur complement models in a flexible way.

The main contribution of this study is to show that the combination of the techniques presented in this article can be used to achieve significant speed benefits when modeling WPT systems. The technique results in a significant drop in the number of DOF and faster solving times in repeated simulations, such as simulating the effects of misalignment of the WPT coils. It can be used as a part of optimization algorithms with moving coils in order to find new coil topologies that have better efficiency and misalignment tolerance.

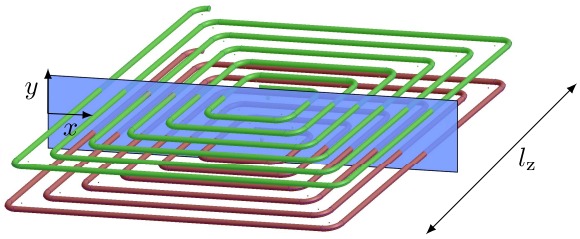

Fig. 1. Rectangular spiral WPT winding and the cross section. Each litz wire and its strands are modeled in the 2-D FE model of the system. Color in electronic version.

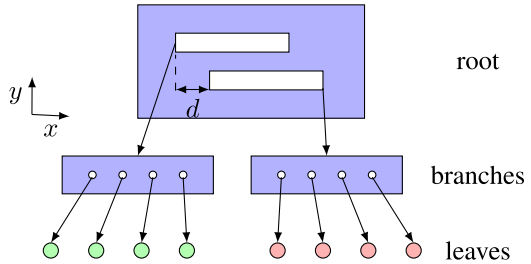

Fig. 2. Diagram of a model tree of a WPT setup (with only two turns for clarity). The leaves are litz wire cross sections, the branches are cross sections of windings with holes for the litz wires, and the root is an air domain with holes for both coils. The symbol d is the offset. Color in electronic version.

II. Methods

A. Decomposition Principle

A WPT unit that consists of two windings is considered (see Fig. 1). The windings are identical, and they have six turns of litz wire. The number of strands in the litz wires is varied from 7 to 925 while keeping the total copper cross section constant. We model the system using a time-harmonic 2-D cross-sectional FE approach with magnetic vector potential. In this approach, transversal symmetry is assumed, and hence, the vector potential has only an out-of-plane component.

The proposed decomposition strategy produces a tree of models. In substructuring methods, this tree is called an elimination tree, and it describes the order in which the inner nodes of the models can be eliminated. In the proposed approach, the building of the discretization for the whole model is avoided completely. Instead, the elimination tree is first created, each submodel is discretized separately, lower level submodels are embedded using the mortar method, and, finally, the inner DOF are eliminated. The tree is illustrated in Fig. 2. It has three different levels of models that are denoted, in this article, as the root, branch, and leaf models. In the decomposition tree, there can be only one root model that is the topmost one and does not have a parent model. Branch models have a single parent model and one or more submodels. A leaf model has only a parent model but no submodels. It is possible to reuse an existing model in the model tree. Only one litz wire model can be used for all wires in the coil.

Each submodel in the model tree is responsible for providing its parent a precomputed mapping of itself. The tree below the submodel is incorporated in this precomputed mapping. Hence, the geometric details present in the tree below are not visible to the parent model. A cross-sectional model requires that the currents of the wires are mapped between the cross sections according to the winding geometry. A common approach is to use the AVI formulation where an external circuit model is used to connect the cross sections of the strands together. This adds some complexity on the top of a standard domain decomposition technique.

The construction of the total system proceeds by traversing the model tree from the leaves to the root. It is noteworthy that, in this approach, precomputed models can be reused in multiple ways. For example, a leaf level model (a litz wire) can be embedded multiple times into a branch level model to create a model of a litz winding. It is enough to create, mesh, and pre-process only one litz wire cross section model. In Sections II-B to D, we go through how a time-harmonic AVI formulation for a three-level model tree is constructed.

B. Litz Wire as a Leaf Model

A litz wire consists of multiple thin strands that are isolated from each other and indexed with index l. The total current entering the wire gets distributed between the strands. A strand is thought to be a conductive solid tube, and the voltage over the tube acts as a source to a quasistatic field problem where magnetic vector potential is used. The standard commonly used AVI formulation [24] that is fed with current can be expressed as

$$\begin{bmatrix} \mathbf{K} & \mathbf{C}_\mathrm{J} & \mathbf{0} \\ j\omega\mathbf{C}_\mathrm{E} & -\mathbf{I} & \mathbf{RL} \\ \mathbf{0} & \mathbf{0} & \mathbf{I} \end{bmatrix} \begin{bmatrix} \mathbf{a} \\ \mathbf{u} \\ \mathbf{i} \end{bmatrix} = \begin{bmatrix} \mathbf{0} \\ \mathbf{0} \\ \mathbf{i}_\mathrm{s} \end{bmatrix} \tag{1}$$

where $\omega = 2\pi f$, where f is the frequency, j is the imaginary unit, $\mathbf{K} = \mathbf{S} + j\omega\mathbf{M}$, where $\mathbf{S}$ is the magnetic stiffness matrix emerging from both the non-conductive and conductive domains ($\Omega^\mathrm{L}_\mathrm{a}$ and all $\Omega^\mathrm{L}_{\mathrm{c},l}$) of the litz wire domain represented in Fig. 3, and $\mathbf{M}$ is the eddy-current damping matrix, which emerges from the conductive domains (only $\Omega^\mathrm{L}_{\mathrm{c},l}$). The superscript L denotes the litz domain. Symbol $\mathbf{a}$ represents the nodal values of the z-component of the magnetic vector potential, $\mathbf{u}$ represents the voltages over the strand tubes in the z-direction, and $\mathbf{i}$ represents the strand currents.

The matrix $\mathbf{C}_\mathrm{J}$ is computed as

$$[\mathbf{C}_\mathrm{J}]_{il} = -\frac{\sigma}{l_z}\int_{\Omega^\mathrm{L}_{\mathrm{c},l}} \psi_i \, d\Omega^\mathrm{L}_{\mathrm{c},l} \tag{2}$$

where σ is the conductivity of copper, l_z is the length in the symmetric z-direction (see Fig. 1), ψ_i is the ith FE basis function, and $\Omega^\mathrm{L}_{\mathrm{c},l}$ is the domain of the lth strand (see Fig. 3). The matrix $\mathbf{C}_\mathrm{E}$ is computed as

$$[\mathbf{C}_\mathrm{E}]_{li} = -\frac{l_z}{|\Omega^\mathrm{L}_{\mathrm{c},l}|}\int_{\Omega^\mathrm{L}_{\mathrm{c},l}} \psi_i \, d\Omega^\mathrm{L}_{\mathrm{c},l} \tag{3}$$

where $|\Omega^\mathrm{L}_{\mathrm{c},l}|$ is the area of the domain $\Omega^\mathrm{L}_{\mathrm{c},l}$.

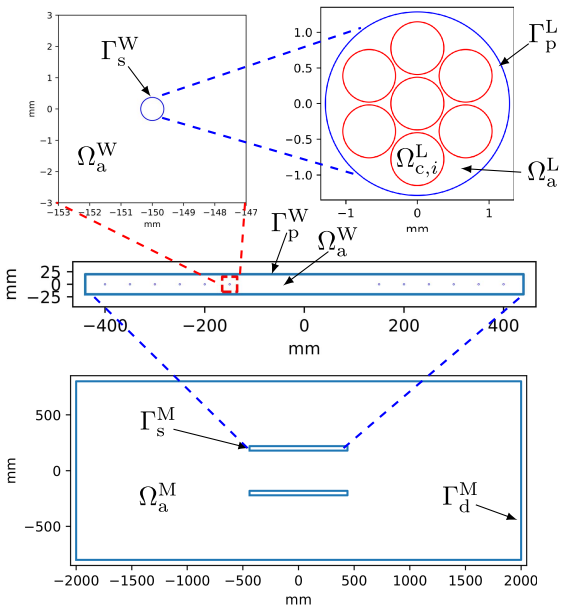

Fig. 3. Cross sections of a litz wire, winding, and the total domain. The red dashed line represents a magnification, and the blue dashed lines represent a mortar mapping where the boundaries Γ^i_s from a parent model i and Γ^j_p from a submodel j are glued together. The symbol $\Omega^\mathrm{L}_\mathrm{a}$ denotes the insulation, which is assumed to behave magnetically like a vacuum, $\Omega^\mathrm{W}_\mathrm{a}$ denotes the former of the winding, here assumed to be air, and $\Omega^\mathrm{M}_\mathrm{a}$ denotes the air around the windings. Color in electronic version.

The matrix $\mathbf{R} = \mathrm{diag}(R_1, \ldots, R_{n_\mathrm{s}})$, where n_s is the number of strands, is a diagonal matrix of the resistances of the strand tubes, which are computed as

$$R_l = \frac{l_z}{\sigma|\Omega^\mathrm{L}_{\mathrm{c},l}|} \tag{4}$$

for strand l. $\mathbf{L}$ is a matrix where

$$[\mathbf{L}]_{lk} = \begin{cases} 1, & \text{current } i_k \text{ flows through } l \text{ forward} \\ -1, & \text{current } i_k \text{ flows through } l \text{ backwards} \\ 0, & \text{otherwise} \end{cases} \tag{5}$$

i.e., it maps strand currents to the cross sections of the conductors in the litz wire.

The last row and column of the matrix in (1) are associated with the external circuit equations that are related to the winding structure, i.e., how the strands connect to each other and how many turns there are. In a current-fed model, the strand currents flowing through the strand cross sections can be set directly using $\mathbf{i}_\mathrm{s}$. The strand currents are included in the state vector for convenience. Treating the strand currents separately would result in a smaller amount of state variables, but this only has an impact on the precomputation step.

System (1) is transformed to the Schur complement form. The DOF in vector $\mathbf{a}$ are decomposed into $\mathbf{a}_\mathrm{i}$ and $\mathbf{a}_\mathrm{p}$ denoting the interior nodes and boundary nodes in the boundary between the litz domain and the parent domain, respectively

$$\begin{bmatrix} \mathbf{K}_\mathrm{ii} & \mathbf{K}_\mathrm{ip} & \mathbf{C}_\mathrm{J} & \mathbf{0} \\ \mathbf{K}_\mathrm{pi} & \mathbf{K}_\mathrm{pp} & \mathbf{0} & \mathbf{0} \\ j\omega\mathbf{C}_\mathrm{E} & \mathbf{0} & -\mathbf{I} & \mathbf{R} \\ \mathbf{0} & \mathbf{0} & \mathbf{0} & \mathbf{I} \end{bmatrix} \begin{bmatrix} \mathbf{a}_\mathrm{i} \\ \mathbf{a}_\mathrm{p} \\ \mathbf{u} \\ \mathbf{i} \end{bmatrix} = \begin{bmatrix} \mathbf{0} \\ \mathbf{0} \\ \mathbf{0} \\ \mathbf{i}_\mathrm{s} \end{bmatrix}. \tag{6}$$

The system (6) can be written as

$$\begin{bmatrix} \mathbf{K}_{ii} & \mathbf{B} \\ \mathbf{C} & \mathbf{D} \end{bmatrix} \begin{bmatrix} \mathbf{a}_i \\ \mathbf{x}^L \end{bmatrix} = \begin{bmatrix} \mathbf{0} \\ \mathbf{f}^L \end{bmatrix} \tag{7}$$

where

$$\mathbf{B} = \begin{bmatrix} \mathbf{K}_{ip} & \mathbf{C}_J & \mathbf{0} \end{bmatrix} \tag{8}$$

$$\mathbf{C} = \begin{bmatrix} \mathbf{K}_{pi}^T & j\omega\mathbf{C}_E^T & \mathbf{0}^T \end{bmatrix}^T \tag{9}$$

$$\mathbf{D} = \begin{bmatrix} \mathbf{K}_{pp} & \mathbf{0} & \mathbf{0} \\ \mathbf{0} & -\mathbf{I} & \mathbf{R} \\ \mathbf{0} & \mathbf{0} & \mathbf{I} \end{bmatrix}. \tag{10}$$

From the first row of (7), $\mathbf{a}_i$ can be solved as

$$\mathbf{a}_i = -\mathbf{K}_{ii}^{-1}\mathbf{B}\mathbf{x}^L \tag{11}$$

and substituted to the second row of (7) to obtain

$$\underbrace{\left(\mathbf{D} - \mathbf{C}\mathbf{K}_{ii}^{-1}\mathbf{B}\right)}_{=\mathbf{G}^L}\mathbf{x}^L = \mathbf{f}^L \tag{12}$$

where

$$\mathbf{G}^L = \begin{bmatrix} \mathbf{G}_{11}^L & \mathbf{G}_{12}^L & \mathbf{0} \\ \mathbf{G}_{21}^L & \mathbf{G}_{22}^L & \mathbf{R} \\ \mathbf{0} & \mathbf{0} & \mathbf{I} \end{bmatrix} \tag{13}$$

and its blocks are

$$\mathbf{G}_{11}^L = \mathbf{K}_{pp} - \left(\mathbf{K}_{pi}\mathbf{K}_{ii}^{-1}\mathbf{K}_{ip}\right) \tag{14}$$

$$\mathbf{G}_{12}^L = -\mathbf{K}_{pi}\mathbf{K}_{ii}^{-1}\mathbf{C}_J \tag{15}$$

$$\mathbf{G}_{21}^L = -j\omega\mathbf{C}_E\mathbf{K}_{ii}^{-1}\mathbf{K}_{ip} \tag{16}$$

$$\mathbf{G}_{22}^L = -\mathbf{I} - j\omega\mathbf{C}_E\mathbf{K}_{ii}^{-1}\mathbf{C}_J. \tag{17}$$

The remaining state vector is

$$\mathbf{x}^L = \begin{bmatrix} \mathbf{a}_p^T & \mathbf{u}^T & \mathbf{i}^T \end{bmatrix}^T \tag{18}$$

and the source vector is

$$\mathbf{f}^L = \begin{bmatrix} \mathbf{0}^T & \mathbf{0}^T & \mathbf{i}_{in}^T \end{bmatrix}^T. \tag{19}$$

The vectors are presented in transposed form for brevity.

The mapping $\mathbf{G}^L$ is what is meant by a precomputed mapping that characterizes the litz wire cross section completely. It can be precomputed independently and reused later. The state vector $\mathbf{x}^L$ will be visible for the parent model, but all other variables ($\mathbf{a}_i$ in this case) are eliminated. The vector $\mathbf{a}_i$ can be recovered from the state vector $\mathbf{x}^L$ by using (11).

C. Winding as a Branch Model

A winding consists of multiple turns of a conductor. The six turns in the rectangular spiral winding result in 12 litz wire domains in the cross section of the winding. We assume that there are no core materials or other conducting materials than the litz wires in the winding domain. The litz wires have been cut out from the geometry. The cross section is obtained by doing a cut in the xy-plane as in Fig. 1, and the length l_z is the length to the transversal symmetric direction.

After FE discretization, the matrix equation of the air domain Ω_a^W in the winding cross section can be written as

$$\mathbf{S}^W\mathbf{a}^W = \mathbf{0} \tag{20}$$

since there are no source fields in this model as the litz wire domains are not included. The superscript W denotes the winding domain.

A voltage-fed AVI formulation is used as a starting point in the winding level. This is written as

$$\begin{bmatrix} \mathbf{K} & \mathbf{C}_J & \mathbf{0} \\ j\omega\mathbf{C}_E & -\mathbf{I} & \mathbf{RL} \\ \mathbf{0} & \mathbf{L}^T & \mathbf{Z}_{ew} \end{bmatrix} \begin{bmatrix} \mathbf{a} \\ \mathbf{u} \\ \mathbf{i} \end{bmatrix} = \begin{bmatrix} \mathbf{0} \\ \mathbf{0} \\ \mathbf{u}_{in} \end{bmatrix} \tag{21}$$

where $\mathbf{Z}_{ew}$ contains the end winding impedances. The last row of (21) contains the circuit equations connecting the strands of each cross section to each other through voltage equations. In the third row, the voltages over the windings can be set using $\mathbf{u}_{in}$.

The internal nodes in the domain are separated from the boundary nodes in such a way that we distinctively separate the boundary to the parent model and the boundaries to the submodels. We also plug in the submodel systems by following the approach presented in [31] that is based on the mortar method with the Lagrange multipliers denoted with $\mathbf{b}^W$. The total system then takes the form

$$\begin{bmatrix} \mathbf{S}^W & \mathbf{0} & \mathbf{0} & \mathbf{0} & \mathbf{D}_i^H \\ \mathbf{0} & \mathbf{G}_s^W & \mathbf{0} & -\mathbf{L}_i^W & -\mathbf{D}_s^H \\ \mathbf{0} & \mathbf{L}_u^W & -\mathbf{I} & \mathbf{Z}_{ew} & \mathbf{0} \\ \mathbf{0} & \mathbf{0} & \mathbf{I} & \mathbf{0} & \mathbf{0} \\ \mathbf{D}_i & -\mathbf{D}_s & \mathbf{0} & \mathbf{0} & \mathbf{0} \end{bmatrix} \begin{bmatrix} \mathbf{a}^W \\ \mathbf{x}_s^W \\ \mathbf{u}_g^W \\ \mathbf{i}_g^W \\ \mathbf{b}^W \end{bmatrix} = \begin{bmatrix} \mathbf{0} \\ \mathbf{0} \\ \mathbf{0} \\ \mathbf{u}_{in} \\ \mathbf{0} \end{bmatrix} \tag{22}$$

where the superscript H denotes a conjugate transpose and the block matrices are defined as follows. The zeroes in most of the sparse matrices are left out for clarity.

The stiffness matrix part $\mathbf{S}^W$ is decomposed into internal node parts and boundary node parts, and its structure is

$$\mathbf{S}^W = \begin{bmatrix} \mathbf{S}_{ii}^W & \mathbf{S}_{ip}^W & \mathbf{S}_{is,1}^W & \cdots & \mathbf{S}_{is,12}^W \\ \mathbf{S}_{pi}^W & \mathbf{S}_{pp}^W & & & \\ \mathbf{S}_{si,1}^W & & \mathbf{S}_{ss,1}^W & & \\ \vdots & & & \ddots & \\ \mathbf{S}_{si,12}^W & & & & \mathbf{S}_{ss,12}^W \end{bmatrix} \tag{23}$$

where $\mathbf{S}_{ii}^W$ contains the entries related to the interior nodes, $\mathbf{S}_{ip}^W$ contains the entries connecting the interior nodes and the nodes at the parent model boundary, $\mathbf{S}_{is,k}^W$ and $\mathbf{S}_{si,k}^W$ contain the entries connecting the interior nodes and the nodes at the boundary to the kth submodel, and the diagonal blocks $\mathbf{S}_{pp}^W$ and $\mathbf{S}_{ss,k}^W$ correspond to the entries connecting the boundary nodes in the parent boundary and submodel boundary to each other, respectively. The block $\mathbf{G}_s^W$ in (22) is

$$\mathbf{G}_s^W = \begin{bmatrix} \mathbf{G}_1^L & & \\ & \ddots & \\ & & \mathbf{G}_{12}^L \end{bmatrix} \tag{24}$$

where $\mathbf{G}_k^L$ corresponds to the block of the precomputed mapping (12) of the kth litz wire subdomain.

The $\mathbf{f}^L$ term (19) contains the strand currents that flow through the strands in the litz wire model, and it has been

moved to the left-hand side. The term $\mathbf{i}_{\text{in}}$ can be computed from the winding level strand currents as

$$\mathbf{i}_{\text{in}} = \mathbf{L}\mathbf{i}_{\text{g}}^{\text{W}} \tag{25}$$

with the strand current mapping (5). With suitable zero padding, $\mathbf{f}^{\text{L}}$ is represented using a matrix multiplication with $\mathbf{x}^{\text{L}}$ of each subdomain

$$\mathbf{f}^{\text{L}} = \mathbf{L}_{\text{i}}^{\text{W}}\mathbf{x}^{\text{L}} \tag{26}$$

where

$$\mathbf{L}_{\text{i}}^{\text{W}} = \begin{bmatrix} \mathbf{0} & \mathbf{0} & \mathbf{L}^{\text{T}} & \dots & \mathbf{0} & \mathbf{0} & \mathbf{L}^{\text{T}} \end{bmatrix}^{\text{T}}. \tag{27}$$

This results in the term $-\mathbf{L}_{\text{i}}^{\text{W}}$ in (22). The matrix $\mathbf{L}_{\text{u}}^{\text{W}}$ contains strand current mappings (5) for each subdomain block that maps all the subdomain voltages to the global strand voltages

$$\mathbf{L}_{\text{u}}^{\text{W}} = \begin{bmatrix} \mathbf{0} & \mathbf{L}^{\text{T}} & \mathbf{0} & \dots & \mathbf{0} & \mathbf{L}^{\text{T}} & \mathbf{0} \end{bmatrix}. \tag{28}$$

The matrix $\mathbf{Z}_{\text{ew}} = \text{diag}(Z_1, \dots, Z_{n_{\text{s}}})$ contains the external impedances of each strand in the winding, e.g., the end winding parts. By changing the block rows corresponding to $\mathbf{u}_{\text{g}}^{\text{W}}$ and $\mathbf{i}_{\text{g}}^{\text{W}}$ in (22), and the number of voltages and currents, we can change the connection topology of the winding to, e.g., parallelly connected turns.

The matrices $\mathbf{D}_{\text{i}}$ and $\mathbf{D}_{\text{s}}$ contain the mortar mappings that connect the magnetic fields of the winding domain and the litz wire subdomains. The mappings $\mathbf{D}_{\text{i}}^{\text{W}}$ are the mortar mappings defined in $\Gamma_{\text{p}}^{\text{W}}$ of each winding domain, and $\mathbf{D}_{\text{s}}^{\text{L}}$ are mortar mappings defined in $\Gamma_{\text{s}}^{\text{L}}$

$$\mathbf{D}_{\text{i}} = \begin{bmatrix} \mathbf{0} & \mathbf{0} & \mathbf{D}_{1}^{\text{W}} & & \\ \vdots & \vdots & & \ddots & \\ \mathbf{0} & \mathbf{0} & & & \mathbf{D}_{12}^{\text{W}} \end{bmatrix} \tag{29}$$

$$\mathbf{D}_{\text{s}} = \begin{bmatrix} \mathbf{D}_{1}^{\text{L}} & \mathbf{0} & \mathbf{0} & & & \\ & & & \ddots & & \\ & & & & \mathbf{D}_{12}^{\text{L}} & \mathbf{0} & \mathbf{0} \end{bmatrix}. \tag{30}$$

It must be emphasized that the mappings $\mathbf{D}_{\text{i}}^{\text{W}}$ completely define the way how the subdomains are connected to the parent domain. By changing only these mappings, it is possible to change the way the subdomain connects to the parent domain.

The state vector is also defined in blocks. The first block corresponds to the magnetic problem in the coil domain

$$\mathbf{a}^{\text{W}} = \begin{bmatrix} \mathbf{a}_{\text{i}}^{\text{T}} & \mathbf{a}_{\text{p}}^{\text{T}} & \mathbf{a}_{\text{s,1b}}^{\text{T}} & \cdots & \mathbf{a}_{\text{s,12b}}^{\text{T}} \end{bmatrix}^{\text{T}} \tag{31}$$

where $\mathbf{a}_{\text{i}}$ are the nodal values of the vector potential in the inner nodes, $\mathbf{a}_{\text{p}}$ are the nodal values at the external boundary to the parent model, and $\mathbf{a}_{\text{s},k\text{b}}$ are the nodal values at the boundary of the kth subdomain.

The second block contains the states of the subdomains

$$\mathbf{x}_{\text{s}}^{\text{W}} = \begin{bmatrix} \mathbf{a}_{1}^{\text{T}} & \mathbf{u}_{1}^{\text{T}} & \mathbf{i}_{1}^{\text{T}} & \cdots & \mathbf{a}_{12}^{\text{T}} & \mathbf{u}_{12}^{\text{T}} & \mathbf{i}_{12}^{\text{T}} \end{bmatrix}^{\text{T}} \tag{32}$$

where $\mathbf{a}_k$ are the nodal values of the magnetic vector potential at the kth subdomain's boundary and $\mathbf{u}_k$ are the strand voltages of the kth subdomain.

The third block contains all voltages over the whole strand loops

$$\mathbf{u}_{\text{g}}^{\text{W}} = \begin{bmatrix} u_1 & \cdots & u_{n_{\text{s}}} \end{bmatrix}. \tag{33}$$

The fourth block contains all winding level strand currents

$$\mathbf{i}_{\text{g}}^{\text{W}} = \begin{bmatrix} i_1 & \cdots & i_{n_{\text{s}}} \end{bmatrix} \tag{34}$$

and the block $\mathbf{b}^{\text{W}}$ contains all Lagrange multipliers used to enforce the continuity over the mortar boundaries

$$\mathbf{b}^{\text{W}} = \begin{bmatrix} \mathbf{b}_{1}^{\text{T}} & \cdots & \mathbf{b}_{12}^{\text{T}} \end{bmatrix}^{\text{T}} \tag{35}$$

where $\mathbf{b}_k$ are the Lagrange multiplier values of the kth subdomain boundary. Finally, on the right-hand side, we have $\mathbf{u}_{\text{in}}$ that is a vector of voltages over the whole length of the strands that act as an input for the winding.

Solving the precomputed mapping from (22) is done similarly as in the case of the litz wire slice. We pick the state vector that we want to expose to the parent model as

$$\mathbf{x}^{\text{W}} = \begin{bmatrix} \mathbf{a}_{\text{p}}^{\text{T}} & \left(\mathbf{u}_{\text{g}}^{\text{W}}\right)^{\text{T}} & \left(\mathbf{i}_{\text{g}}^{\text{W}}\right)^{\text{T}} \end{bmatrix}^{\text{T}}. \tag{36}$$

The rest of the state variables are packed in a vector $\mathbf{x}_{\text{i}}^{\text{W}}$, and the system is rearranged into the following form:

$$\begin{bmatrix} \mathbf{A} & \mathbf{B} \\ \mathbf{C} & \mathbf{D} \end{bmatrix} \begin{bmatrix} \mathbf{x}_{\text{i}}^{\text{W}} \\ \mathbf{x}^{\text{W}} \end{bmatrix} = \begin{bmatrix} \mathbf{0} \\ \mathbf{f}^{\text{W}} \end{bmatrix} \tag{37}$$

where $\mathbf{A}$, $\mathbf{B}$, $\mathbf{C}$, and $\mathbf{D}$ contain the entries from the system matrix of (22), which are picked from the rows and columns to match the state variables in $\mathbf{x}_{\text{i}}^{\text{W}}$ and $\mathbf{x}^{\text{W}}$. The source term is

$$\mathbf{f}^{\text{W}} = \begin{bmatrix} \mathbf{0} & \mathbf{0} & \mathbf{u}_{\text{in}}^{\text{T}} \end{bmatrix}^{\text{T}}. \tag{38}$$

Next, the system is taken into the Schur complement form. The term $\mathbf{x}_{\text{i}}^{\text{W}}$ can be solved from the first row of (37) as

$$\mathbf{x}_{\text{i}}^{\text{W}} = -\mathbf{A}^{-1}\mathbf{B}\mathbf{x}^{\text{W}} \tag{39}$$

and this can be inserted to the second row of (37) to obtain

$$\underbrace{\left(\mathbf{D} - \mathbf{C}\mathbf{A}^{-1}\mathbf{B}\right)}_{\mathbf{G}^{\text{W}}} \mathbf{x}^{\text{W}} = \mathbf{f}^{\text{W}}. \tag{40}$$

Here, the mapping $\mathbf{G}^{\text{W}}$ is the precomputed mapping that completely describes this model and all its submodels. Only the variables in the state vector $\mathbf{x}^{\text{W}}$ are exposed to the parent model. It is noteworthy that the states of the submodels and the Lagrange multipliers related to submodels get eliminated, and they are not visible to the parent model. The solution inside the subdomain can be recovered from the reduced state by using (39).

D. WPT Setup as Root Model

The highest level, i.e., the root model, is a magnetoquasistatic problem containing the surroundings and placement of the windings. In this level, we model the air region around the windings and connect two or possibly more winding subdomains using the mortar method. The root model is after FE discretization writable as (20). The approach is similar to that in the branch level model that we assemble an equation system, including the mortar equations. However, at the root level, we do not have to do the precomputation step; instead, we will enforce a Dirichlet boundary condition to the outer boundary of the domain.

The root model system can be written as

$$\begin{bmatrix} \mathbf{S}_i^M & \mathbf{0} & \mathbf{D}_i^H \\ \mathbf{0} & \mathbf{G}_s^M & -\mathbf{D}_s^H \\ \mathbf{D}_i & -\mathbf{D}_s & \mathbf{0} \end{bmatrix} \begin{bmatrix} \mathbf{a}_i^M \\ \mathbf{x}_s^M \\ \mathbf{b}^M \end{bmatrix} = \begin{bmatrix} \mathbf{0} \\ \mathbf{f}^M \\ \mathbf{0} \end{bmatrix} \tag{41}$$

where

$$\mathbf{S}_i^M = \begin{bmatrix} \mathbf{S}_{ii} & \mathbf{S}_{s,1b} & \mathbf{S}_{a,2b} \\ \mathbf{S}_{s,b1} & \mathbf{S}_{s,11} & \mathbf{0} \\ \mathbf{S}_{a,b2} & \mathbf{0} & \mathbf{S}_{s,22} \end{bmatrix} \tag{42}$$

consists of the entries corresponding to nodes in the area surrounding the coils and the boundaries to the winding slots

$$\mathbf{G}_s^M = \begin{bmatrix} \mathbf{G}_1^W & \mathbf{0} \\ \mathbf{0} & \mathbf{G}_2^W \end{bmatrix} \tag{43}$$

contains the precomputed submodel blocks of the windings

$$\mathbf{D}_i = \begin{bmatrix} \mathbf{0} & \mathbf{D}_1^M & \mathbf{0} \\ \mathbf{0} & \mathbf{0} & \mathbf{D}_2^M \end{bmatrix} \tag{44}$$

is the mortar matrix of the root model side, and

$$\mathbf{D}_s = \begin{bmatrix} \mathbf{D}_{s1}^W & \mathbf{0} & \mathbf{0} & & & \\ & & & \mathbf{D}_{s2}^W & \mathbf{0} & \mathbf{0} \end{bmatrix} \tag{45}$$

is the mortar matrix of the subdomain side. The superscript M denotes the main domain. The state vector consists of blocks

$$\mathbf{a}_i^M = \begin{bmatrix} \mathbf{a}_i^T & \mathbf{a}_{s,1b}^T & \mathbf{a}_{s,2b}^T \end{bmatrix}^T \tag{46}$$

where $\mathbf{a}_i$ are the nodal values inside the domain and $\mathbf{a}_{s,1b}$ and $\mathbf{a}_{s,2b}$ are the nodal values at the boundaries to the upper and lower coil domains, respectively. The subdomain state block

$$\mathbf{x}_s^M = \begin{bmatrix} \left(\mathbf{x}_1^W\right)^T & \left(\mathbf{x}_2^W\right)^T \end{bmatrix}^T \tag{47}$$

consists of the states of the subdomains of upper and lower coils, respectively. The block $\mathbf{b}^M$ contains the Lagrange multipliers for each subdomain

$$\mathbf{b}^M = \begin{bmatrix} \mathbf{b}_1^T & \mathbf{b}_2^T \end{bmatrix}^T. \tag{48}$$

The right-hand side has a block $\mathbf{f}^M$ that is used to specify the source voltages over the windings

$$\mathbf{f}^M = \begin{bmatrix} \left(\mathbf{f}_1^W\right)^T & \left(\mathbf{f}_2^W\right)^T \end{bmatrix}^T. \tag{49}$$

The construction has the benefit that the DOF visible in any model in the tree consist of only the DOF of the model itself, the DOF related to Lagrange multipliers, and the boundary nodes of its submodels. The DOF inside the problem domain of the submodel are eliminated from the total system. The resulting equation system, which is linear in this linear problem, can be solved using a direct solver, and the results in the subdomains can be recovered directly from the reduced states by using (39) for each subdomain. The total process of building a decomposed model is summarized in Fig. 4.

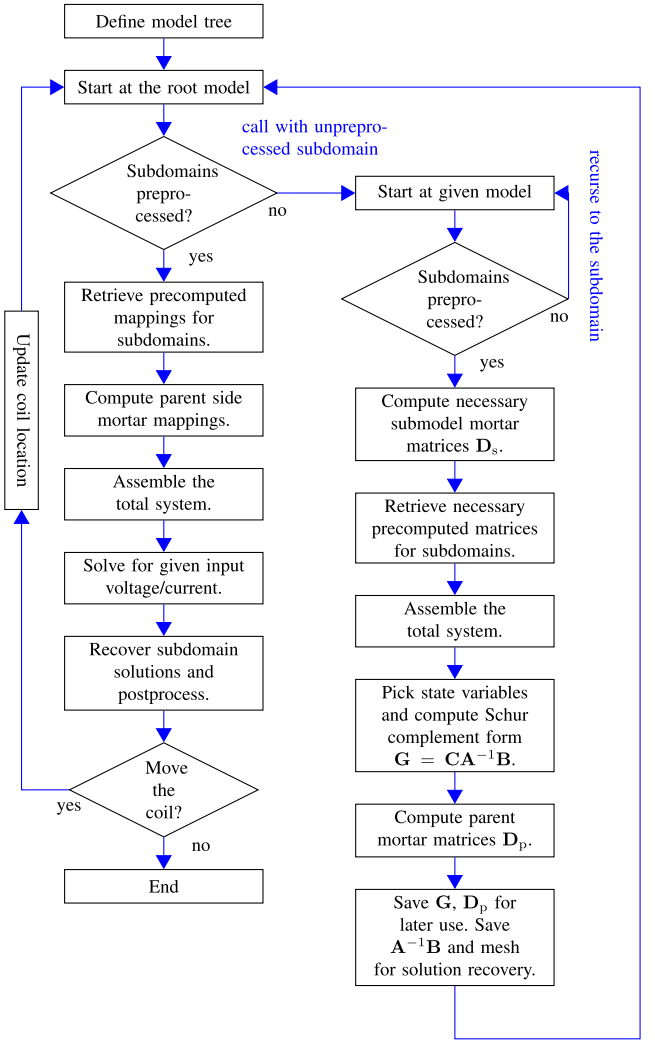

Fig. 4. Flowchart that summarizes the solution process. The symbols $\mathbf{G}$, $\mathbf{D}_s$, and $\mathbf{D}_p$ denote the precomputed Schur complement matrices, mortar matrices for the boundaries facing a subdomain, and mortar matrices for the boundaries facing the parent domain, respectively.

TABLE I
DESIGN PARAMETERS OF THE WPT SYSTEM

Winding outer diameter	800 mm
Winding inner diameter	300 mm
Transfer distance	400 mm
Number of turns	6
Litz copper cross section	3 mm^2
Operating frequency	120 kHz

III. RESULTS

The generation of eddy current losses inside the litz wires with different numbers of strands is simulated for a WPT unit whose design parameters are given in Table I. The series–series compensation topology is used because its resonance frequency is independent of the load and the coupling coefficient [3]. The coupling coefficient k is computed as

$$k = \frac{M}{\sqrt{L_1 L_2}} \tag{50}$$

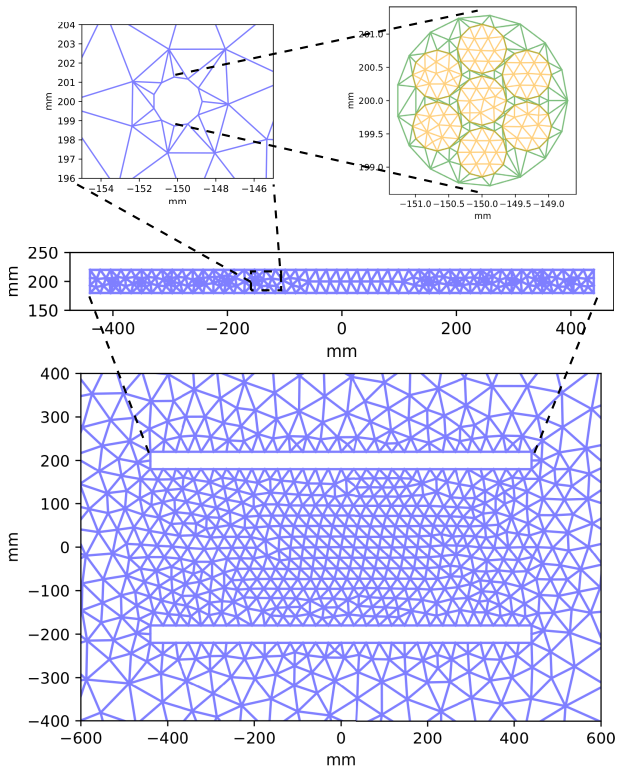

Fig. 5. Meshes of the decomposed domains. For clarity, the meshes here are sparser than the meshes used in the computations. Also, the root domain has been cropped from the original width and height. Each domain has been meshed separately. The same meshes are reused for the lower coil slot.

where M is the mutual inductance between the windings and L_1 and L_2 are the self-inductances of the receiving and sending coils.

A. FE Simulations

The decomposed model is verified against a traditional FE simulation where each strand is modeled individually for as many strands as possible until the traditional simulation turns infeasible; 51 different winding positions were simulated, in which the horizontal offset d (see Fig. 2) between the primary and secondary coils varied from 0 to 400 mm. The litz wire geometries are generated using hexagonal packing, and only symmetric configurations were used. The studied strand numbers were 7, 19, 31, 55, 85, 109, 151, 199, 241, 301, 349, 421, 499, 559, 649, 733, 823, and 925. The cross-sectional area of the strands was chosen so that the total copper cross-sectional area remained constant at 3.0 mm^2. The traditional FE model turned infeasible after 199 strands, while the decomposed approach allowed simulations up to higher values.

The operating frequency was chosen to be 120 kHz. The decomposition technique does not have limitations regarding the frequency. It shares similar properties than a standard quasistatic FE formulation: capacitive effects are neglected, and meshes in conductive regions need to be dense enough to account for skin effect.

The meshes used in the decomposed simulation are constructed, as presented in Fig. 5. In the decomposed version, each domain has been meshed separately. In the traditional version, the whole geometry, including all strands, was meshed all at once. The meshes in Fig. 4 are for illustrational purposes, and denser meshes were used in the actual simulations. The average lengths of element edges were $4.41 \cdot 10^{-2}$, 4.43, and 29.4 mm in the litz wire, winding domain, and root domain, respectively, in seven strands. The lengths were determined by the strand diameter d_s such that the edge length was set to $(d_s/20)$ in the litz strands. The mesh densities were set to be equal at the domain boundaries in both traditional and decomposed cases to obtain comparable results. This makes the meshes close to conforming, so the accuracy is the highest. This also provides a worst case scenario considering the performance. The meshes could be made sparser over the boundaries with reasonable accuracy, and it would speed up the decomposed computations [31].

The FE simulations were run in a 30BES18S00 Lenovo ThinkStation P520 with 192-GB RAM. The equation systems were solved with SuperLU direct solver. For a higher number of strands than 199, the traditional simulation started to take a considerable amount of time and memory. In the decomposed approach, the amount of DOF in the root level FE system stays the same, but there are two DOF per strand coming from the voltage and current of the strand. Hence, the root level total system grows linearly with the number of strands. The solvers are implemented on top of an in-house FE toolkit written with Python, and the geometry and meshing are done using GMSH:s Python API.

The results in Table II show that the proposed technique yields a model that is significantly faster to update and re-solve than the implemented traditional FE approach. The numbers of DOF in the decomposed side contain only DOF in the final system of the root model. There is also some growth as a function of n_s in the numbers of decomposed DOF. One reason is that each strand is visible at the root level as two DOF: one for the voltage and one for the current. Also, when the element size needs to be decreased in the strand level with respect to the strand size, the element size in the parent models needs to be decreased slightly to avoid generating meshes of bad quality. This effect is especially visible in the extreme case of 925 strands, and it could be countered by sparsening the meshes over the mortar boundaries.

The solving time contains the solving of the equation system and the extraction of the net currents in both scenarios. The remeshing column shows the time needed to remesh the regions that are affected by the change of alignment of coils. In the traditional approach, the whole domain needs to be remeshed; in the decomposed approach, only the root model is remeshed. From this, it can be concluded that if the total simulation needs to be repeated many times, the proposed technique is faster, especially with litz wires with a high number of strands. The precomputations can be cached to further reduce the need for recomputation.

B. Loss Analysis

At the system level, an equivalent circuit model presented in Fig. 6 is used. The eddy-current losses are included in the winding resistances R_1 and R_2 that depend on frequency and position of the coils. The resistive load that gives the highest

TABLE II
PRECOMPUTATION TIMES, AVERAGE NUMBERS OF DOF, AND AVERAGE RUNTIMES PER STEP OF THE FE SIMULATIONS

	Traditional			Decomposed			
n_s	DOF	Remeshing (s)	Solve (s)	Precomp. (s)	DOF	Remeshing (s)	Solve (s)
7	126616	7.30	3.35	12.22	14262	0.71	0.42
19	276527	7.30	3.35	12.78	14310	0.71	0.42
85	1047441	77.03	43.40	26.37	14574	0.72	0.42
199	2363706	238.70	128.50	71.99	15030	0.72	0.54
925	-	-	-	911.28	17934	0.73	1.02

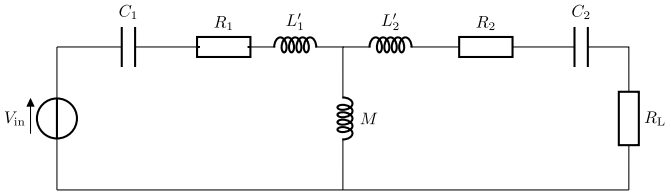

Fig. 6. Equivalent circuit for the WPT system with series–series compensation. The stray inductances in the circuit are $L_1' = L_1 - M$ and $L_2' = L_2 - M$.

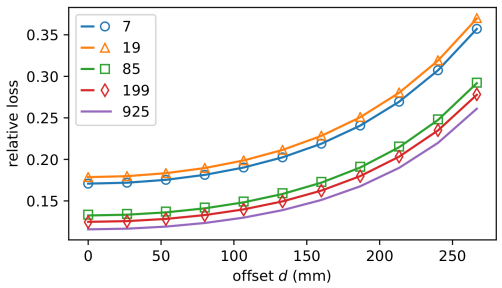

Fig. 7. Relative loss $1-\eta$, where η is the efficiency with respect to alignment and number of strands. Solid lines denote the results obtained through the decomposed approach, and markers denote the results obtained through a traditional FE approach. Color in electronic version.

efficiency can be solved from the equivalent circuit as

$$R_L = \sqrt{\frac{R_2}{R_1}\left(L_1 L_2 k^2 \omega_0^2 + R_1 R_2\right)} \tag{51}$$

where $\omega_0 = 2\pi f_0$, where f_0 is the supply frequency, chosen to be equal to the resonance frequency.

The lumped parameters, R_1, R_2, L_1, L_2, and M, were identified through the FE simulations. The FE problem was solved twice for each frequency, the number of strands, and alignment. An input rms voltage of 1 V is first set into the sending coil, and the secondary is short-circuited, i.e., rms voltage of 0 V is set over the receiving coil. A second simulation is done with a short-circuited sending coil and an rms voltage 1 V in the receiving coil. The sending and receiving coil currents are then recovered in both cases, and the lumped parameters are then computed using a least-squares fitting from the voltages and the currents. Due to linearity, the powers and losses calculated with FE models and the lumped parameters are equal.

The system is then tuned by computing the compensation capacitances in the position where coils are perfectly aligned using

$$C_i = \frac{1}{\omega_0^2 L_i} \tag{52}$$

where $i = 1, 2$. For each data point, the optimal load resistance R_L is calculated. The efficiency of the WPT system is then computed based on the equivalent circuit.

The results are shown in Fig. 7. It can be seen from the figure that the 19-strand case has slightly worse efficiency due to proximity effects, but the efficiency is, in general, better when the number of strands increases. The results of the decomposed and traditional approach are matching well. There is, in general, less than 1% error in the computed currents used for parameter identification. Hence, it can be concluded that the decomposition does not significantly reduce accuracy.

Operating voltages and currents were obtained from the equivalent circuit model. To make the losses comparable, the net current of the sending coil was forced to 18 A, resulting in an average current density of 6 A/mm^2 in the litz wire of the sending coil. The current densities in the strands were computed to observe the skin effect and proximity effect inside the litz wire, and they are visualized in Fig. 8. To visualize the uneven distribution of losses between the strands, the losses in each strand were computed and plotted in Fig. 9. The loss per strand is inversely proportional to the number of strands. The reference line $(67.97/n_s)$ W (matching the loss at $n_s = 1$) shows how the loss should behave when skin and proximity

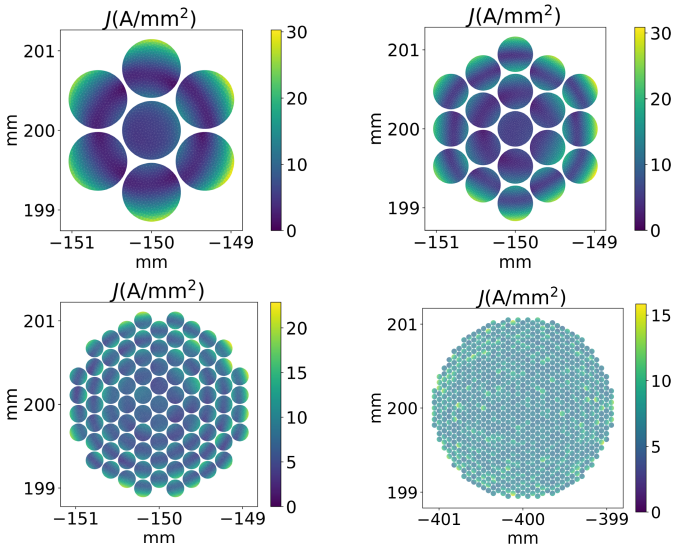

Fig. 8. Reconstructed magnitude of the current density of the cross section of 7-, 19-, 81-, and 925-strand wires at the same position. The scale in each cross section is from 0 A to the maximum value of the current density in the cross section. The reduction of the skin effect is clearly visible when the strand diameter gets smaller.

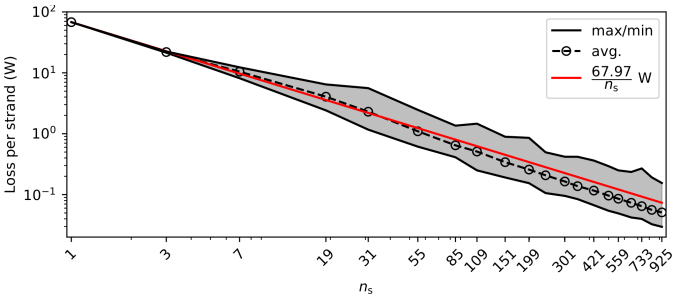

Fig. 9. Losses in sending coil for different amounts of strands in perfect alignment. The solid lines show the maximum and minimum amongst all strands. The dashed line shows the average loss per strand, and the markers show the data points. The red line shows the reference line $(67.97/n_s)$ W, which shows how the loss should behave for a dc current. Both the x- and y-axes are logarithmic.

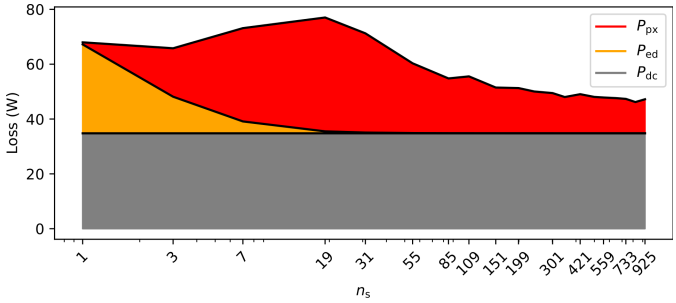

Fig. 10. Losses in the sending coil of the WPT unit separated into dc, skin effect, and proximity losses denoted with P_{dc}, P_{ed}, and P_{px}, respectively. The x-axis is logarithmic. Color in electronic version.

effects are neglected. As the average loss drops below the reference line, it can be concluded that increasing the number of strands reduces the losses in the wire.

The skin and proximity effects were separated by analytically computing the losses purely caused by the skin effect. The ac resistance of an individual strand in the litz wire can be computed as (see [32, eq. (6-14)])

$$R_{\mathrm{s}} = \mathrm{Re}\left\{ \frac{j^{\frac{3}{2}}k}{2\pi r\sigma} \frac{J_0\left(j^{\frac{3}{2}}kr\right)}{J_1\left(j^{\frac{3}{2}}kr\right)} \right\} \tag{53}$$

where r is the strand radius, J_0 and J_1 are the Bessel functions of the first kind of order 0 and 1, respectively, and

$$k = \sqrt{\omega\sigma\mu_0} \tag{54}$$

where μ_0 is the permeability of the free space.

Dividing the total current of 18 A evenly into the strands and applying (53) yield the sum of losses caused by the dc resistance (P_{dc}) and pure skin effect (P_{ed}). The dc loss can be further separated by using only the dc resistance (4). The proximity effect losses are obtained by subtracting the analytically calculated loss from the loss obtained from the FE solution (P_{FE}), which accounts for the uneven distribution of the current between the strands

$$P_{\mathrm{px}} = P_{\mathrm{FE}} - P_{\mathrm{ed}} - P_{\mathrm{dc}}. \tag{55}$$

The different loss components are shown in Fig. 10. It is noteworthy that the loss arising in the lumped-parameter end-winding resistances includes not only dc losses but also proximity losses due to the uneven distribution of the current between the strands.

From the results, it can be seen that, in the sending coil, the dc loss stays constant with respect to the number of strands. This is expected since the current of the sending coil was constant. The skin effect losses decay quickly. The proximity effect of other strands, other turns, and the receiving coil then accounts for the rest of the losses. The proximity losses vary depending on the position of the strands. For the single-strand case, the proximity losses are negligible, which indicates that most of the proximity losses emerge from the interaction between parallel strands, not series turns. On the other hand, increasing the number of strands seems to radically decrease the losses in the wire.

IV. Conclusion

A recursive domain decomposition approach was presented and applied in an efficiency study of a WPT unit. The simulations show that the ac-resistance of a litz wire winding drops when the number of strands increases and the copper cross section is kept constant. The proposed decomposition approach results in a faster and less resource-intensive simulation model than a traditional FE approach. This is beneficial when the model has to be repeatedly solved, e.g., when a parameter sweep is done. It also enables one to model litz wires with an extremely high number of strands without homogenization techniques. In future work, the method could be extended to 3-D problems. The method could also be developed as a part of, e.g., multi-slice methods that could also incorporate capacitive effects.

Acknowledgment

This work was supported in part by the KAUTE Foundation, in part by the Walter Ahlström Foundation, in part by the Emil Aaltonen Foundation, and in part by the European Research Council (ERC) through the European Union's Horizon 2020 Research and Innovation Programme under Grant Agreement 848590.

References

[1] Z. Zhang, H. Pang, A. Georgiadis, and C. Cecati, "Wireless power transfer—An overview," *IEEE Trans. Ind. Electron.*, vol. 66, no. 2, pp. 1044–1058, Feb. 2019.

[2] D. Gunji, K. Hata, O. Shimizu, T. Imura, and H. Fujimoto, "Feasibility study on in-motion wireless power transfer system before traffic lights section," in *Proc. IEEE PELS Workshop Emerg. Technol., Wireless Power Transf. (WoW)*, London, U.K., Jun. 2019, pp. 302–307.

[3] W. Zhang and C. C. Mi, "Compensation topologies of high-power wireless power transfer systems," *IEEE Trans. Veh. Technol.*, vol. 65, no. 6, pp. 4768–4778, Jun. 2016.

[4] G. Wei, X. Jin, C. Wang, J. Feng, C. Zhu, and M. I. Matveevich, "An automatic coil design method with modified AC resistance evaluation for achieving maximum coil–coil efficiency in WPT systems," *IEEE Trans. Power Electron.*, vol. 35, no. 6, pp. 6114–6126, Jun. 2020.

[5] X. Shi, H. Lee, V. Jain, and J. R. Smith, "Coil geometry optimization for wireless power delivery to moving receivers," in *Proc. IEEE Wireless Power Transf. Conf. (WPTC)*, Montreal, QC, Canada, Jun. 2018, pp. 1–4.

[6] M. Bertoluzzo, G. Buja, and H. Dashora, "Avoiding null power point in DD coils," in *Proc. IEEE PELS Workshop Emerg. Technol., Wireless Power Transf. (WoW)*, London, U.K., Jun. 2019, pp. 11–15.

[7] R. Bosshard and J. W. Kolar, "Multi-objective optimization of 50 kW/85 kHz IPT system for public transport," *IEEE J. Emerg. Sel. Topics Power Electron.*, vol. 4, no. 4, pp. 1370–1382, Dec. 2016.

[8] J. H. Kim *et al.*, "Development of 1-MW inductive power transfer system for a high-speed train," *IEEE Trans. Ind. Electron.*, vol. 62, no. 10, pp. 6242–6250, Oct. 2015.

[9] S. Moon and G.-W. Moon, "Wireless power transfer system with an asymmetric four-coil resonator for electric vehicle battery chargers," *IEEE Trans. Power Electron.*, vol. 31, no. 10, pp. 6844–6854, Oct. 2016.

[10] K. Niyomsatian, J. Van den Keybus, R. V. Sabariego, and J. Gyselinck, "Frequency-domain homogenization for litz-wire bundles in finite element calculations," in *Proc. 18th Eur. Conf. Power Electron. Appl. (EPE ECCE Europe)*, Karlsruhe, Germany, Sep. 2016, pp. 1–10.

[11] D. W. Ferreira, R. V. Sabariego, L. Lebensztajn, L. Krahenbuhl, F. Morel, and C. Vollaire, "Homogenization methods in simulations of transcutaneous energy transmitters," *IEEE Trans. Magn.*, vol. 50, no. 2, pp. 1017–1020, Feb. 2014.

[12] J. Gyselinck and P. Dular, "Frequency-domain homogenization of bundles of wires in 2-D magnetodynamic FE calculations," *IEEE Trans. Magn.*, vol. 41, no. 5, pp. 1416–1419, May 2005.

[13] J. Gyselinck, R. V. Sabariego, and P. Dular, "Time-domain homogenization of windings in 2-D finite element models," *IEEE Trans. Magn.*, vol. 43, no. 4, pp. 1297–1300, Apr. 2007.

[14] J. Smajic, J. Hughes, T. Steinmetz, D. Pusch, W. Monig, and M. Carlen, "Numerical computation of ohmic and eddy-current winding losses of converter transformers including higher harmonics of load current," *IEEE Trans. Magn.*, vol. 48, no. 2, pp. 827–830, Feb. 2012.

[15] B. F. Smith, P. E. Bjārstad, and W. D. Gropp, *Domain Decomposition: Parallel Multilevel Methods for Elliptic Partial Differential Equations*. Cambridge, U.K.: Cambridge Univ. Press, 1996, pp. 101–133.

[16] T. J. Barth, T. F. Chan, and W. P. Tang, "A parallel non-overlapping domain-decomposition algorithm for compressible fluid flow problems on triangulated domains," *Contemporary Math.*, vol. 21, pp. 23–41, Jan. 1998.

[17] J. Jønsson, S. Krenk, and L. Damkilde, "Recursive substructuring of finite elements," *Comput. Struct.*, vol. 54, no. 3, pp. 395–404, Feb. 1995.

[18] Y. Zhilichev, "Analysis of permanent magnet machines using crossing macro-elements," *IEEE Trans. Magn.*, vol. 36, no. 5, pp. 3122–3124, Sep. 2000.

[19] K. Smetana and A. T. Patera, "Optimal local approximation spaces for component-based static condensation procedures," *SIAM J. Sci. Comput.*, vol. 38, no. 5, pp. 3318–3356, 2016.

[20] A. Szucs, "Macro elements in the finite element analysis of multiconductor eddy-current problems," *IEEE Trans. Magn.*, vol. 36, no. 4, pp. 813–817, Jul. 2000.

[21] A. C. Cangellaris, "Electromagnetic macro-modeling: An overview of current successes and future opportunities," in *Proc. CEM Comput. Electromagn. Int. Workshop*, Izmir, Turkey, Aug. 2011, pp. 1–6.

[22] K. Nyka, "Diagonalized macromodels in finite element method for fast electromagnetic analysis of waveguide components," *Electronics*, vol. 8, no. 3, p. 260, Feb. 2019.

[23] A. Szucs, "Macro element approach for electromagnetic simulations in multi-physics and system analysis," in *Proc. Int. Symp. Power Electron. Power Electron., Electr. Drives, Autom. Motion*, Sorrento, Italy, Jun. 2012, pp. 700–705.

[24] I. A. Tsukerman, A. Konrad, and J. D. Lavers, "A method for circuit connections in time-dependent eddy current problems," *IEEE Trans. Magn.*, vol. 28, no. 2, pp. 1299–1302, Mar. 1992.

[25] L. Lehti, J. Keranen, S. Suuriniemi, and L. Kettunen, "Coil winding losses: Decomposition strategy," *IEEE Trans. Magn.*, vol. 52, no. 1, Jan. 2016, Art. no. 7000106.

[26] A. Lehikoinen, J. Ikaheimo, A. Arkkio, and A. Belahcen, "Domain decomposition approach for efficient time-domain finite-element computation of winding losses in electrical machines," *IEEE Trans. Magn.*, vol. 53, no. 5, May 2017, Art. no. 7400609.

[27] D. Klis, S. Burgard, O. Farle, and R. Dyczij-Edlinger, "Fast simulation of wireless power transfer systems with varying coil alignment," *IFAC-Papers Line*, vol. 48, no. 1, pp. 248–253, 2015.

[28] F. B. Belgacem, "The mortar finite element method with Lagrange multipliers," *Numerische Math.*, vol. 84, no. 2, pp. 173–197, Dec. 1999.

[29] B. I. Wohlmuth, "A mortar finite element method using dual spaces for the Lagrange multiplier," *SIAM J. Numer. Anal.*, vol. 38, no. 3, pp. 989–1012, Jan. 2000.

[30] S. Falletta, "The approximate integration in the mortar method constraint," in *Proc. 16th Domain Decomposition Methods Sci. Eng.*, vol. 55, 2007.

[31] A. Marjamaki and P. Rasilo, "Domain decomposition technique with subdomain pre-processing in 2-D simulations of wireless power transfer," *IEEE Trans. Magn.*, vol. 56, no. 4, Apr. 2020, Art. no. 7515104.

[32] J. Lammeraner and M. Stafl. (1996). *Eddy Currents*. [Online]. Available: https://archive.org/details/EddyCurrents